J. Mech. Phys. Solids 184 (2024) 105548

Contents lists available at ScienceDirect

Journal of the Mechanics and Physics of Solids

journal homepage: www.elsevier.com/locate/jmps

Enhancing toughness through geometric control of the process zone

Sage Fulco [a], Michal K. Budzik [b,*], Kevin T. Turner [a,*]

[a] Department of Mechanical Engineering and Applied Mechanics, University of Pennsylvania, Philadelphia, PA, USA
[b] Department of Mechanical Engineering and Production, Aarhus University, Aarhus, Denmark

ARTICLE INFO

Keywords:
Architected materials
Plasticity
Toughness
Finite element analysis

ABSTRACT

Material architecture provides an opportunity to alter and control the fracture process zone shape and volume by redistributing the local stresses at a crack tip. Properly designed structures can enlarge the plastic zone and enhance the effective toughness. Here, we use a pillar array as a model structure to demonstrate how variations in geometry at a crack tip control the size and shape of the plastic zone and can be used to engineer the effective toughness. Elastic–plastic finite element simulations are used to quantify how the pillar width, spacing, and height can be varied to tailor the size and shape of the plastic zone. A set of analytical mechanics models that accurately estimate the shape, volume, and resulting toughness as a function of the base material properties and geometry are also presented. A case study extends the analysis to sets of non-regular pillar arrays to illustrate how architecture can be used to alter toughness along the crack path.

1. Introduction

During fracture, high stresses near a crack tip result in a region of inelastic material damage, designated as the fracture process zone. For many materials, this region results from plastic deformation and is referred to as the plastic zone, with larger plastic zones dissipating more energy and resulting in higher fracture toughness. For homogeneous materials, the radius of the plastic zone, r_p, is directly tied to the yield strength of the material, σ_y, such that $r_p \propto (\sigma_y)^{-2}$ (Irwin, 1957). The fracture toughness of a material is often tailored by changing the material composition and microstructure to reduce the yield strength, which increases the plastic zone radius and enhances the toughness. However, there is a trade-off with this approach as there is a loss in strength (Ritchie, 2011). Fine-scale architecture, enabled by additive manufacturing (Bertoldi et al., 2017; Walia et al., 2015; Wegst et al., 2014; Yang et al., 2018; Vyatskikh et al., 2018; Saccone et al., 2022; Gross and Bertoldi, 2019), offers a new mechanism for toughening materials by using geometry to alter the shape and size of the plastic zone. Material architecture has been leveraged to great success in enhancing material properties (Messner, 2016; Ostoja-Starzweski, 2002; Schaedler et al., 2011; Meza et al., 2014; Zheng et al., 2014; Ramachandramoorthy et al., 2020; Ashby, 2005; Pham et al., 2019; Abedi et al., 2021), but has mostly been used to increase stiffness- and strength-to-weight ratios (Schaedler et al., 2011; Meza et al., 2014; Zheng et al., 2014; Ramachandramoorthy et al., 2020; Bauer et al., 2016; Mueller et al., 2018; Park et al., 2020; Compton and Lewis, 2014), or to create materials with high energy absorption under compressive loading (Ashby, 2005; Pham et al., 2019; Abedi et al., 2021; Mohsenizadeh et al., 2018). Most approaches for designing and optimizing mechanical properties have relied on elastic analyses, and material architecture has not yet been widely exploited to increase the fracture toughness of materials, with only some recent works having considered the topic (Heide-Jorgensen et al., 2020; Fulco et al., 2022; Mateos et al., 2019; Zhang and Mao, 2018; Shaikeea et al., 2022; Hossain et al., 2014; O'Masta et al., 2017; Hsueh et al., 2018; Athanasiadis et al., 2021; Luan et al., 2022; Cui et al., 2020; Muro-Barrios et al.,

---

* Corresponding authors.
E-mail addresses: mibu@mpe.au.dk (M.K. Budzik), kturner@seas.upenn.edu (K.T. Turner).

https://doi.org/10.1016/j.jmps.2024.105548
Received 28 June 2023; Received in revised form 2 November 2023; Accepted 9 January 2024

2022). These works have successfully related the topology of the architecture to the failure (Zhang and Mao, 2018; Shaikeea et al., 2022; Cui et al., 2020; Muro-Barrios et al., 2022) and demonstrated use of homogenization methods (Heide-Jorgensen et al., 2020; Mateos et al., 2019), but are limited in that most consider microstructures that fail in an elastic-brittle manner. Many structural materials, including those utilized in additive manufacturing, exhibit significant plasticity during failure. As microstructures are fabricated at increasingly smaller characteristic length scales (Vyatskikh et al., 2018; Saccone et al., 2022; Gross and Bertoldi, 2019) – well below r_p of the material – failure is unlikely to be accurately described by elastic-brittle mechanisms. This limits the applicability of these models to design structures with enhanced fracture properties. As plastic deformation at the crack tip is one of the primary contributions to toughness in homogeneous materials, understanding and leveraging plasticity in structured and architected materials represents a significant opportunity to design materials with enhanced toughness.

Without a better understanding of the role of plasticity in architected materials, potential opportunities for enhancing toughness may be missed. Our recent work (Fulco et al., 2022) is the first we are aware of that examined elastic–plastic fracture of an architected system. Predicting where plasticity will occur, or potentially localize, is complicated in architected systems. Plasticity that is isolated to a particular feature of the structure may lead to a very different failure phenomena and load than if large portions of the structure yield. These failure regimes are controlled by the geometry, the micromechanics of the architecture, and the material's characteristic fracture length scale (Fulco et al., 2022; Kanninen, 1973).

Expanding on the well-established fracture mechanics analyses of homogeneous materials, where the plastic zone shape is known, the objective of this work is to investigate how architecture can be used to intentionally alter the plastic zone shape, and how particular design choices can result in larger plastic zones and increased toughness. A pillar array is used as a model system, which has been discussed on several occasions, including our recent work (Heide-Jorgensen et al., 2020; Fulco et al., 2022). In Fulco et al. (2022), it was shown experimentally that introducing a pillar array along the crack plane of a ductile material could alter the plastic zone shape and enhance the toughness, but the analysis was confined to a limited set of array geometries. Here, the problem is considered in a more general analysis, without limitations to elasticity, as was the case in Heide-Jorgensen et al. (2020), or specific array geometries, as in Fulco et al. (2022). A general framework is developed that can be utilized for materials with a range of elastic–plastic behavior or adapted to other architectures. It is validated through numerical modeling using a material model based on previous experiments that demonstrated how toughness can be enhanced through architecture (Fulco et al., 2022). A pillar array was chosen as a model geometry as the micromechanics are more tractable for predicting the size and shape of the plastic zone, although the fundamental approaches taken in this work are agnostic to the micromechanics and could be applied to more complicated geometries in future investigations. This work presents a general energy analysis for structured elastic–plastic materials, which depends on predicting the plastic zone size and shape. This is achieved for the pillar array through a set of analytical mechanics models that provide an algorithm for predicting the plastic zone size for any array geometry. Results are illustrated and validated through a set of finite element simulations of varying pillar geometries, which demonstrate the ability to vary the plastic zone size and the resulting toughness through changes in pillar width, spacing, and height, and show good agreement with the analytical predictions. Finally, a case study is presented to extend the model to non-regular pillar arrays and demonstrates how toughness can be tuned locally as the crack propagates.

2. Theoretical framework

For the pillar array, an elastic analysis (Heide-Jorgensen et al., 2020) previously demonstrated that arrays with increased compliance result in a more uniform stress along the interface. This improves the effective toughness of the structured material, since greater stress uniformity leads to a lower stress in the first pillar (i.e., the "crack tip") for a given load. In our recent work (Fulco et al., 2022), it was shown experimentally that this could be leveraged to an even greater degree when a material deforms plastically, since the increased compliance results in a larger plastic zone, and proportionally more energy dissipation. That work was limited to cases where plastic deformation only existed in the pillar array. Here, we build on the previous work by presenting a new general elastic–plastic model that can predict the plastic zone shape and volume, as well as the resulting toughness, and is demonstrated for a general set of pillar array geometries. These models are verified through finite element simulations (see Section 3).

2.1. Model geometry

This work considers the effect of the geometry of a structured region in the crack plane of a compact tension (CT) specimen (ASTM, 2020; ASTM International, 2007), as shown in Fig. 1(a). For homogeneous elastic–plastic materials, a plastic zone will form around the crack tip, with the typical (plane strain) shape shown in Fig. 1(b). A regular pillar array, as shown in Fig. 1(c & d), is introduced along the crack plane, and is parameterized by four dimensions: the pillar height, t, pillar width, l_x, pillar spacing, s_x, and fillet radius, r. In 2-D, this system looks like a pillar, although we note that the plane strain model can accommodate pillars of varying width, b, and is not restricted to pillars with cross-sectional areas that have aspect ratios close to one. The length scale of the pillar dimensions is on the order of the plastic zone radius of the material or smaller. Additional details of the range of dimensions for each parameter used in this work are discussed in the finite element model description below. Due to the compressive region near the far boundary of the CT specimen, if a crack is too long, or the pillar geometry results in a plastic zone that is too large, the compressive field can impede the development of the plastic zone and artificially reduce the toughness (ASTM International, 2007). Throughout this work, geometries were limited to only those where the plastic zone was fully developed and away from the boundary before failure.

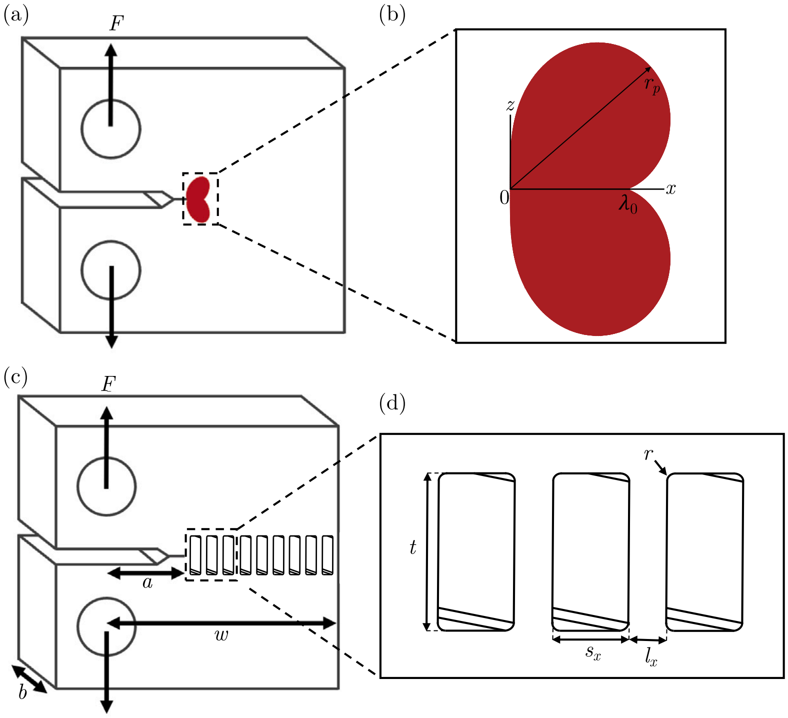

Fig. 1. (a) Homogeneous compact tension specimen with plastic zone shown (in red); (b) Plane strain plastic zone of a homogeneous mode I fracture specimen, with the radius, r_p, and the plastic zone extension, λ_0, indicated. (c) Compact tension specimen geometry with pillar interface. (d) Pillar interface in crack region of CT specimen, corresponding to outlined region in (c), showing pillar spacing, s_x, width, l_x, height, t, and fillet radius, r.

2.2. *Toughness of an architected material*

Energy-based analyses of fracture define the toughness of a material as its critical energy release rate, G_c, which for a brittle material is equivalent to the rate of energy per unit crack area required to create the two surfaces of a crack. For a brittle material with surface energy γ, the critical energy release rate is $G_c = 2\gamma$ (Griffith, 1921). In most cases there are additional dissipative mechanisms, such as plasticity, and these significantly increase G_c. In these cases, the toughness is then typically denoted instead by J. To understand the role of plasticity, consider the potential energy, Π, of a specimen with domain Ω as

$$\Pi = \int_{\Omega} u_e dV + \int_{\Omega} u_p dV + \int_{\Gamma} \gamma dA - W, \qquad (1)$$

where u_e is the elastic energy density, u_p is the plastic energy density, W is the external work done, and $\Gamma = 2A$ is the crack surface area, with $A = ab$, where a and b are the crack length and specimen width, respectively, as shown in Fig. 1(c). Taking the first variation of the potential energy with respect to crack area and setting equal to zero (i.e., $\frac{\partial \Pi}{\partial A} = 0$) and noting that the plastic energy is confined to the plastic zone, Ω_p, the toughness of the material, J^*, is defined as

$$J^* \equiv -\frac{\partial}{\partial A}\left(\int_{\Omega} u_e dV - W\right) = \frac{\partial}{\partial A}\left(\int_{\Omega_p} u_p dV\right) + 2\gamma, \qquad (2)$$

where J^* is used to indicate an effective toughness measurement, and $\frac{\partial}{\partial A}\int_{\Gamma} \gamma dA = 2\gamma$. Note that the derivative of the plastic integral is conservative only if the plastic zone size is unchanged during crack propagation, as is assumed here. This analysis of the architected specimen follows that of the homogeneous case, but Ω_p may not follow the plastic zone shape of a homogeneous specimen, but instead will be a function of the pillar geometry. Given that the following analysis does not follow some assumptions of traditional fracture mechanics such as continuity (Lubliner, 1990), we refer to J^* as an effective toughness measurement.

Assuming the fracture is self-similar (i.e., $\frac{dJ^*}{da} = 0$), which implies self-similarity of the plastic zone, the plastic energy term will be proportional to the plastic zone volume, with $\int_{\Omega_p} u_p dV = \bar{\rho}_p \Omega_p$, with $\bar{\rho}_p = \int_{\epsilon} K\epsilon^m d\epsilon$ being the average plastic energy density, where K and m are material properties, the plastic modulus and hardening exponent, respectively. For a regular and repeating pillar interface, the assumption of a conservative plastic integral is assumed to be satisfied if the plastic zone is of the same volume for any $a = a_0 + i(l_x + s_x)$, for $i = 1, 2, \ldots, n$, with n being the number of repeated features and a_0 being the initial crack length. This approach does not explicitly account for the elastic strain energy recovered from the plastic domain during unloading. This elastic energy is expected to be small compared to the plastic dissipation. The model can therefore be rigorously applied to predict crack initiation. Under these assumptions, the toughness can be found through the relationship

$$J^* = \Omega_p \frac{\partial}{\partial A}\left(\bar{\rho}_p\right) + 2\gamma, \tag{3}$$

which shows that the toughness can be predicted from three values: Ω_p, $\bar{\rho}_p$, and γ. Note that 2γ is typically much smaller than the plastic term for materials with significant plasticity. Since $\bar{\rho}_p$ and γ depend on the constitutive behavior and intrinsic material properties, they would have to be uniquely identified for every material. However, if the toughness of the array is considered relative to that of a homogeneous specimen of the same material with toughness $J_0 = \Omega_0 \frac{\partial}{\partial A}\left(\bar{\rho}_p\right) + 2\gamma$, where Ω_0 is the plastic volume of the homogeneous specimen, and $\bar{\rho}_p$ and γ are identical to the pillar case, the relative effective toughness can be approximated as

$$\frac{J^*}{J_0} \approx \frac{\Omega_p}{\Omega_0} + \delta_e, \tag{4}$$

where $\delta_e = 2\gamma/J_0$ and 2γ is assumed to be negligible relative to the plastic energy. This assumption results in a linear scaling of toughness with respect to plastic domain, where δ_e is a small offset due to elastic energy. This analysis follows that for a homogeneous material, but is novel in its application when considering the case of an architected material where the size and shape of the plastic zone may be altered. If the toughness of the homogeneous material, J_0, and the size of the plastic zones of the homogeneous and architected specimens are known, the toughness can be predicted.

In our recent work on pillar arrays (Fulco et al., 2022), it was shown that there exists a critical pillar height, t_c, above which plasticity becomes isolated to the pillar array. For planar structures, this critical pillar height, t_c, was found to be $t_c = \mathcal{O}(\lambda_0)$, where λ_0 is the plastic extension during fracture of a homogeneous specimen (Kanninen, 1973) (see Fig. 1(b)). In the case of $t > t_c$, Eq. (4) is simplified as the plastic zone is confined to the plastic region of the pillar array and $\Omega_p = N_p l_x t b$, where N_p is the number of plastically deforming pillars in the array. As discussed in Fulco et al. (2022), in this case the toughness could be estimated even more simply, and scaled with plastic area in the crack plane, or $N_p l_x b$. This estimation was found to be effective when the process zone was confined to the interface and the effective stiffness of the system was reduced proportionally to the pillar height, t. Thus, in the case of plasticity being fully confined to the pillar region, we can approximate the toughness as

$$\frac{J^*}{J_0} \approx \frac{N_p l_x}{\lambda_0} + \delta_0, \tag{5}$$

where δ_0 is an offset due to elastic effects. This analysis is only valid when $t > t_c$ and the pillars are far enough apart so as not to interact (Fulco et al., 2022). For geometries which result in a plastic zone that is not confined to the array, a different analysis is required to predict the plastic zone volume.

2.3. Plastic zone geometry

For an isotropic homogeneous fracture specimen under mode I loading, the shape of the plastic zone (assuming plane strain conditions) can be defined in polar coordinates as the domain $\mathcal{R} \in \{r \leq r_p(\theta), 0 \leq \theta \leq 2\pi\}$ (Lubliner, 1990), with

$$r_p = \left(\frac{K_{IC}}{\sigma_y}\right)^2 \cos^2\left(\frac{\theta}{2}\right)\left[5 - 3\cos(\theta)\right], \tag{6}$$

where r_p is the plastic radius, K_{IC} is the critical mode I stress intensity factor (the fracture toughness), σ_y is the yield strength, and θ is the angle measured from the plane of the crack, directed ahead of the crack tip. This plastic zone shape is shown in Fig. 1(a & b). We will refer to extent of the plastic zone along the crack path in a homogeneous specimen, $\lambda_0 \equiv r_p(0)$, as the *plastic zone extension*.

2.3.1. Foundation model for predicting plastic extension

In the case of a pillar array, the plastic zone extension, λ_p, can be predicted using a foundation model, specifically, a modified Winkler (Dillard et al., 2018) foundation, where the CT bulk is modeled as a Timoshenko beam supported by a piece-wise foundation that is either un-bonded, perfectly plastic, or elastic, corresponding to the three regions of the CT specimen: the traction-free cracked region, the plastic zone near the crack tip, and the elastic region outside the plastic zone, respectively. In the case that plasticity is localized to the pillar array (i.e., no plasticity exists in the CT bulk) this model would be a suitable homogenization of the problem. In cases where the plastic zone includes regions outside the pillar array, the foundation model is a reasonable approximation, provided the plastic zone areas in the CT bulk do not cause significant deviations from elastic beam theory. However, the model no longer provides a route to directly calculate the plastic volume, Ω_p, but can be used in conjunction with other models to determine its value, as shown in Section 2.3.2.

The elastic-perfectly plastic foundation model considered here has (Dillard et al., 2018) equilibrium equations

$$\frac{dM}{dx} + V = 0, \quad \frac{dV}{dx} - b\sigma(x) = 0, \tag{7}$$

where $M = EI\frac{d\phi}{dx}$ is the bending moment, $V = \kappa G A_b\left(\frac{dw}{dx} - \phi\right)$ is the shear force with w the beam deflection and ϕ the rotation, E is the Young's modulus, $I = bh^3/12$ is the moment of inertia with h the beam height and b the beam width, G is the shear modulus, A_b is the cross-sectional area of the beam, and $\kappa \approx 5/6$ is the shear coefficient. $\sigma(x)$ is a piecewise function describing the foundation, where $\sigma(x) = 0$ in the cracked region, $\sigma(x) = fb\sigma_y$, in the perfectly plastic region, where $f = l_x/(l_x + s_x)$ is the pillar array area fraction, and $\sigma(x) = kw$ in the elastic region, where $k = \left(\frac{2b}{t}E\right) f$ is the foundation stiffness.

As indicated in Fig. 1, the cracked region extends from the loading point ($x = 0$) to the crack tip ($x = a$). The perfectly plastic region then extends from the crack tip to the furthest extent of the plastic zone along the crack plane ($x = a + \lambda_p$), with the remaining region corresponding to the elastic foundation. As has been shown previously (Heide-Jorgensen et al., 2020), in the cracked region, the bending moment is $M = -Px$ and the shear force, $V = -P$, which results in rotation

$$\phi_1 = -\frac{P}{2EI}x^2 + A_1, \tag{8}$$

where A_1 is a constant of integration, and the subscript $()_i$ refers to the solution in the ith region, (1) the cracked domain, (2) the plastic domain, and (3) the elastic domain. The deflection in the cracked region can then be found to be

$$w_1 = \frac{P}{6EI}x^3 + \frac{P}{\kappa GA}x + A_1 x + B_1, \tag{9}$$

where B_1 is another constant of integration. In the perfectly plastic region, the shear force can be found via integration to be $V = fb\sigma_y x^2 + A_2$, and the moment is then found to be $M = -\frac{1}{2} fb\sigma_y x^2 - A_2 x + B_2$, where A_2 and B_2 are also constants of integration. The equilibrium equations (Eq. (7)) can then be solved to find the rotation

$$\phi_2 = 12EI\left(-\frac{1}{3} fb\sigma_y x^3 - A_2 x^2 + 2B_2 x\right) + C_2, \tag{10}$$

and the deflection

$$w_2 = 124EI\left(12B_2 x^2 - 4A_2 x^3 - fb\sigma_y x^4\right) + \frac{1}{2AG\kappa}\left(fb\sigma_y x^2 + 2A_2 x\right) - C_2 x + D_2, \tag{11}$$

where C_2 and D_2 are constants of integration. Finally, the elastic region can be solved by combining the equilibrium equations into a fourth-order differential equation (Heide-Jorgensen et al., 2020) for the deflection,

$$EI\frac{d^4w}{dx^4} + \frac{EIk}{\kappa AG}\frac{d^2w}{dx^2} = kw(x) \tag{12}$$

which has a general solution of the form

$$w_3 = A_3 e^{-\gamma_1 x} + B_3 e^{\gamma_1 x} + C_3 e^{-\gamma_2 x} + D_3 e^{\gamma_2 x} \tag{13}$$

where A_3, B_3, C_3, and D_3 are unknown constants, $\gamma_1 = \Lambda\sqrt{2(\epsilon + \sqrt{\epsilon^2 - 1})}$, $\gamma_2 = \Lambda\sqrt{2(\epsilon - \sqrt{\epsilon^2 - 1})}$, with $\Lambda = \left(\frac{k}{4EI}\right)^{1/4}$ and $\epsilon = \frac{\sqrt{kEI}}{2\kappa GA}$. The significance of these constants has been discussed previously in Heide-Jørgensen and Budzik (2017) and Salem et al. (2013).

To simplify the problem, the specimen is assumed to be infinitely long with no deformation at the boundary, implying $B_2 = D_2 = 0$. This assumption will lead to a slight over-prediction of the plastic zone length compared to the compact tension specimen, where compression must be present near the boundary. The remaining unknown constants can be solved for by requiring continuity of the deformation, rotation, and shear angle.

To find the plastic zone length, λ_p, the stress in the elastic region of the foundation is calculated from the deflection, and the position where it equals the effective yield strength, $f\sigma_y$, can then be determined. For comparison to finite element results, it is useful to convert this length to the number of plastically deforming pillars, as $N_p = \lambda_p/(l_x + s_x)$. For the case where plasticity is isolated to the pillar array, the plastic zone volume can then be directly predicted as the number of plastically deforming pillars multiplied by the volume of a pillar:

$$\Omega_p = N_p l_x tb = \lambda_p \frac{l_x}{l_x + s_x} tb. \tag{14}$$

For geometries where the plasticity is not confined to the array, this model can be extended to account for the plastic domain outside of the array.

2.3.2. Perturbation model for predicting plastic domain outside the pillar array

To account for plasticity outside of the pillar array, we propose a simple model based on the following assumptions: (1) the stress state in the bulk is agnostic to the micromechanics inside the pillar array and depends only on the applied stress state along the boundaries between the array and the bulk, and (2) if the pillar array geometry were to converge towards a solid material (i.e., $s_x/l_x \to 0$), the shape of the plastic zones in the bulk would resemble that of a homogeneous specimen. Under these assumptions, the analysis of the plastic domain can be considered in two parts, the plastic domain in the pillars and the plastic domain in the CT bulk. The total plastic volume is the sum of the plastic volume of the pillar array and the plastic volume in the bulk.

To predict the size of the plastic domain in the CT bulk, we propose a perturbation analysis for estimating the area of the plastic zone, which is proportional to the volume through the thickness. The pillar array is taken as a foundation (that is infinitely thin) between the two CT bulk regions with a prescribed stress state (i.e., a uniform yield stress for an elastic-perfectly plastic material) over the length of the plastic zone along the crack path. This length must be equivalent to the number and length of the plastically deformed unit cells of the pillar region, $N_p(l_x + s_x)$. Thus, in polar coordinates with the origin at the crack tip (Fig. 1(b)), a new plastic radius in the bulk, $r^*(\theta)$ is achieved, with the form $r^* = r_p + r_{per}$, where r_{per} is a perturbation of the original plane strain plastic zone radius, r_p, given in Eq. (6). Since the length of the new plastic zone is known, it is clear that $r^*(0) = \lambda_p = N_p(l_x + s_x)$.

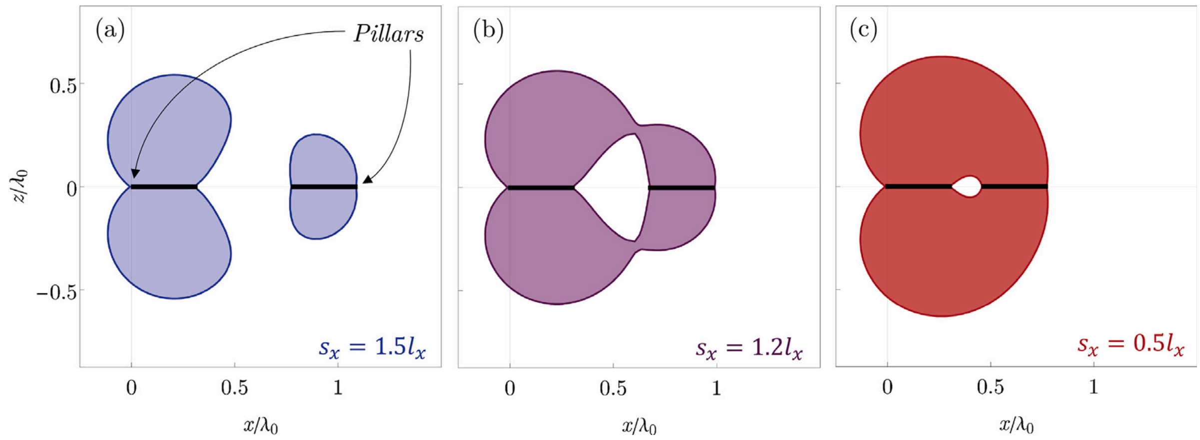

Fig. 2. Regions of bulk plasticity for pillars with spacings (a) $s_x = 1.5l_x$,(b) $1.2l_x$, and (c) $0.5l_x$. The black lines correspond to the pillars, which are taken as infinitely thin regions with prescribed stress states. It is clear that at $s_x = 1.2l_x$ the regions above two pillars combine into a continuous region. For all plots, $\sigma_f = 2\sigma_y$.

A quadratic perturbation in θ is considered, with the perturbation decaying to 0 as $\theta \to \pi$ to ensure that the plastic area converges to the crack tip. This results in a new plastic radius of the form

$$r^* = r_p + r_{per} = \frac{K_{IC}^2}{4\pi\sigma_y^2}\left[\cos^2\left(\frac{\theta}{2}\right)(5 - 3\cos(\theta)) + \zeta(\pi - |\theta|)^2\right] \tag{15}$$

where ζ is a weighting parameter for the perturbation. To ensure that $r^*(0) = N_p(l_x + s_x)$, it is prescribed that $\zeta = 4N_p(l_x + s_x)\left(\frac{\sigma_y^2}{\pi K_{IC}^2}\right) - \frac{2}{\pi^2}$. The area of the plastic zone in the bulk, Ω_p^*, can be then found by integrating, giving

$$\Omega_p^* = \frac{1}{2}\int_0^{2\pi} r^* d\theta = \frac{K_{IC}^2}{\sigma_y^2}\left[\frac{1}{7680\pi}(1845 + 40(39 + 14\pi^2)\zeta + 96\pi^4\zeta^2)\right]. \tag{16}$$

The total size of the plastic zone, Ω_p, is then equal to the sum of the bulk plastic domain and the array plastic domain, $\Omega_p = N_p l_x t b + \Omega_p^*$. Considered relative to the plastic volume of a homogeneous specimen results in

$$\frac{\Omega_p}{\Omega_0} = \frac{N_p(l_x t b)}{\Omega_0} + \left[1 + \frac{8}{369}(39 + 14\pi^2)\zeta + \left(\frac{32\pi^2}{615}\right)\zeta^2\right]. \tag{17}$$

2.3.3. *Plastic zone domains*

The two previous analyses allow for a prediction of the plastic zone domain in two cases, when the plastic zone is isolated to the pillar array ($\Omega_p = \lambda_p l_x t b/(l_x + s_x)$) and when it includes plasticity in the CT bulk ($\Omega_p = (\lambda_p l_x t b/(l_x + s_x)) + \Omega_p^*$). In order to estimate the domain, it must be determined under which conditions plasticity exists in the CT bulk. In the region of the bulk above any plastically deforming pillar, there will be some additional region of plastic deformation. Predicting the exact shape of this region is difficult and would require a full plasticity analysis that is beyond the scope of this work, but the shapes can be approximated using an elastic analysis. Treating the stresses transferred by the pillar as a traction applied to an (2-D) elastic half-space (the CT bulk) (Timoshenko and Goodier, 1934), the stresses will be

$$\sigma_{p_x} = -\frac{q}{\pi}\left[\alpha + \sin(\alpha)\right] \tag{18}$$

$$\sigma_{p_z} = -\frac{q}{\pi}\left[\alpha - \sin(\alpha)\right] \tag{19}$$

where $\alpha(x,z)$ is the angle between two lines drawn from the edges of the pillar to an intersecting point (x,z) (following coordinate system shown in Fig. 2), and $q = \sigma_a l_x/b$, where σ_a is the applied traction due to the pillar, with $\sigma_y \le \sigma_a \le \sigma_f$, where σ_y is the yield strength and σ_f is the failure strength of the material.

Considering two neighboring pillars with the corner of one pillar at the origin, then, by superposition, the stress field in the bulk will be

$$\sigma_x = \sigma_{p_x}(q, x - \frac{l_x}{2}, z) + \sigma_{p_x}(q, x - \frac{3l_x}{2} + s_x, z) + \sigma_b(x,z) \tag{20}$$

and

$$\sigma_z = \sigma_{p_z}(q, x - \frac{l_x}{2}, z) + \sigma_{p_z}(q, x - \frac{3l_x}{2} + s_x, z), \tag{21}$$

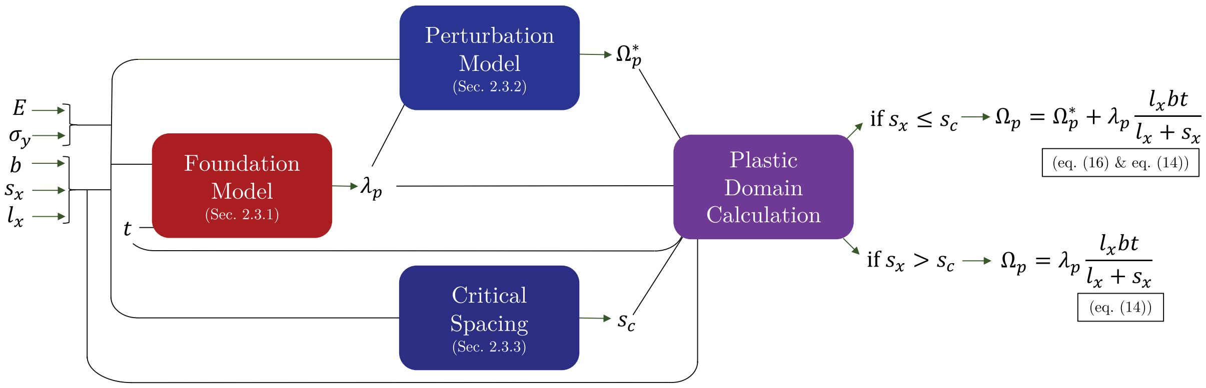

Fig. 3. Graphical representative of the algorithm used in this work to determine the plastic domain. Geometric parameters, t, s_x, and l_x and material properties, E and σ_y, are provided to the foundation model, which calculates the plastic extension, λ_p, and the critical pillar spacing, s_c. If $s_x > s_c$ as determined in Section 2.3.3, plasticity is assumed to be isolated to the pillars and the area can be calculated via Eq. (14); if $s_x \leq s_c$, it is assumed that plasticity exists in the CT bulk, which is then calculated via the perturbation model (Eq. (16)).

where $\sigma_b(x, z) = Mz/I$ is the bending stress in the CT bulk. Since the stresses decay away from the pillars, if the pillars are spaced sufficiently far apart their fields will not interact; but as the spacing decreases, the two fields will combine. As noted above, as the spacing of the pillars goes to zero, it is assumed that a continuous region of plasticity exists along the interface between the pillars and the CT bulk. To identify the critical spacing such that a continuous plastic region exists between two pillars, we identify the case where the von Mises stress, calculated by the superimposed fields, is greater than or equal to the yield strength for at least one value of z at every x coordinate between the pillars. This depends on the value of the applied traction, σ_a. Assuming $\sigma_a = \sigma_f$ and $\sigma_f = 2\sigma_y$ (which is a good model for the material considered in this work, as discussed below in Section 3), three example spacings are shown in Fig. 2, with $s_x = 1.5l_x, 1.2l_x$, and $0.5l_x$. It is clear how two separate plastic zones (i.e., $s_x = 1.5l_x$) combine into a continuous region for smaller spacings. The critical value where a continuous region exists can be solved for numerically as $s_c \approx 1.2l_x$, as shown in the figure. This model is an approximation, and does not account for how plasticity in the bulk might affect the stress decay or for effects from stress concentrations at the corners of the pillars. The corners in this work are filleted ($r = 0.2$ mm) to minimize the effect of stress concentrations. If a perfectly sharp corner were used, it is possible that failure would occur at the pillar-bulk interface, limiting the toughness of the system, but this analysis is outside the scope of this work.

Thus, to predict the plastic domain, we use a simple algorithm that takes as input the geometric parameters, b, l_x, s_x, and t, and material properties, E and σ_y, and calculates the plastic extension using the foundation model and the critical spacing, s_c. If $s_x > s_c$, the plastic volume is just $\Omega_p = \lambda_p l_x tb/(l_x + s_x)$. If $s_x \leq s_c$, then we assume there is significant plasticity in the CT bulk and the plastic volume is calculated as $\Omega_p = [\lambda_p l_x tb/(l_x + s_x)] + \Omega_p^*$ (see Eq. (16)). This process is summarized in Fig. 3.

2.3.4. *Strength and toughness of pillar arrays*

It is important to contextualize any change in toughness in a system by the effect it has on the strength, which are typically inversely related (Ritchie, 2011). As noted in Fulco et al. (2022), architected materials provide opportunities to overcome these traditional trade offs. For a pillar array, the effective tensile strength, σ^*, relative to the strength of a solid material, σ_f, is simply the relative area of the pillars to the whole, f, or

$$\frac{\sigma^*}{\sigma_f} = f = \frac{l_x}{l_x + s_x}. \tag{22}$$

Choices of pillar geometries will impact the strength of the system, but may not affect the toughness in the same way. As found in Fulco et al. (2022), pillar height can affect the toughness of the array, but does not affect strength (Eq. (22)). This provides the opportunity to alter the strength and toughness independently through variations in geometry.

3. Numerical model

Implicit finite element simulations of the CT specimen (Fig. 1) were performed using Abaqus-v6.9 (Dassault Systemes, Velizy-Villacoublay, FR) in 2-D under assumed plane-strain conditions. A spectrum of geometries of the pillar array were considered following a 3-D parameter space with the dimensions varying between $0.5 \leq s_x \leq 4$ mm, $0.5 \leq l_x \leq 2.5$ mm, and $1.5 \leq t \leq 5$ mm, all in step sizes of 0.5 mm. The largest pillar width was chosen so as to remain smaller than the process zone extension of a homogeneous specimen. Geometries that resulted in the pillar at the far boundary being less than the prescribed width were rejected (25 of the possible 96 geometries), resulting in a total of 71 unique geometries. The corners of all pillars were filleted with $r = 0.2$ mm to ensure failure occurs in the pillar, not at the pillar-bulk interface.

Table 1
Tensile and fracture properties of SLS PA 12 used for all numerical models in this work (Fulco et al., 2022).

Modulus, E (GPa)	1.54
Yield strain, ϵ_y (–)	0.02
Yield stress, σ_0 (MPa)	24.8
Hardening, n (–)	8.075
Failure strain, ϵ_f (–)	0.11
Failure stress, σ_f (MPa)	61.8
Toughness, J_0 (kJ/m^2)	6.0
Plastic zone volume, Ω_0 (mm^3)	251.5

A rate-independent elastic–plastic material was simulated using a J_2 deformation plasticity (nonlinear elasticity) model (Lubliner, 1990), which is sufficient for this case since unloading is not considered. The following 1-D power law model is used of the form

$$E\epsilon = \sigma + \epsilon_y \left(\frac{|\sigma|}{\sigma_0} \right)^{n-1} \sigma, \tag{23}$$

where E is the Young's modulus, ϵ is the uniaxial strain, σ is the uniaxial stress, ϵ_y is the yield offset, σ_0 is the effective yield stress, and n is the hardening exponent. Since the introduced architecture eliminates a sharp crack and the crack propagates by pillar rupture, the model does not require a damage model. Failure is defined through the constitutive relationship in Eq. (23), and a failure strain, ϵ_f. This simulation approach removes possible bias introduced through tuning of failure models, and is more computationally efficient.

While the theoretical analysis in this work could be applied to a variety of materials, it requires knowing either the average plastic energy density, $\bar{\rho}_p$, and the elastic fracture energy, γ, or knowing the plastic zone volume, Ω_0 and the toughness, J_0. In this work, we will consider one representative material in the simulations, with properties obtained from measurements of selectively laser sintered Polyamide 12 (SLS PA 12). The experimentally measured plastic zone volume and toughness of the material were reported in our previous work (Fulco et al., 2022). The tensile and fracture properties reported in that work are summarized in Table 1, and were used in Eq. (23) for all finite element simulations in this work.

Failure in the simulations was idealized through a strain-based criterion where the tensile strain in the pillars was equal to the failure strain given in Table 1. Since each pillar was essentially under tensile loading and the pillar dimensions were constrained such that the process zone always spanned the width of the first pillar, this was sufficient to capture failure. A maximum 5% of strain energy is allowed as a stabilization damping energy during failure in all simulations, which has been shown to be sufficient when simulating unstable decay (Gao and Bower, 2004). Simulation data was truncated to the onset of failure, which corresponded to the first pillar of the array reaching its failure strain, so stabilization cannot have any significant effect on the results used. Simulations were run under displacement boundary conditions with a prescribed maximum displacement of 5 mm (all specimens failed before achieving this displacement). Simulations were run with a dynamic time step with a maximum step size corresponding to 0.1 mm of displacement and a minimum step size of 10^{-15} mm. All simulations used 4-node quadrilateral elements with a mesh size in the bulk of 0.25 mm, and a mesh size in the pillar region of 0.10 mm. The mesh in the bulk and the pillars was chosen through a convergence study which resulted in less than 0.5% deviation in the potential energy of the system and the work applied, and in the failure load. Reduced integration elements were used. A comparison between a simulated pillar array and an experimental specimen tested in Fulco et al. (2022) is shown in Appendix and demonstrates the numerical model's fidelity to the experimental material.

The reaction load from the loading points in the CT bulk and the corresponding displacement were measured and saved for each simulation. For both this work and Fulco et al. (2022), the effective toughness of the material is determined through the critical load achieved immediately before the first pillar fails, F_c. This is a measurable quantity that allows for relative comparisons between geometries. We calculate the effective toughness as

$$J^* = F_c^2 \left(\frac{Y^2}{E^* b^2 w} \right), \tag{24}$$

where $E^* = \frac{E}{1-\nu^2}$ is the plane strain modulus, and $Y \equiv Y(\frac{a}{w})$ is defined in ASTM International (2007) for a compact tension geometry in mode I fracture. There is currently no accepted approach for evaluating the toughness of architected materials with geometric length scales comparable to the fracture length scale. Linear elastic fracture mechanics and the J-integral assume a continuous body (Lubliner, 1990) that is violated by these geometries. The effective toughness measurement, when normalized by the toughness of a homogeneous specimen, reduces to $J^*/J_0 \approx (F_c/F_0)^2$, where F_0 is the failure load for the homogeneous specimen. This normalized effective toughness is equal to the relative load capacity between the architected and homogeneous specimens squared, thus providing a comparison between the performance of different designs.

4. Results and discussion

Results for three representative geometries ($t = 2, l_x = 1, s_x = 2, 1, 0.5$ mm) are given in Fig. 4, showing the von Mises stress distributions (sub-figures a–c) and associated plastic zone shapes (sub-figures d–f). Plastic zone area was analyzed by taking an

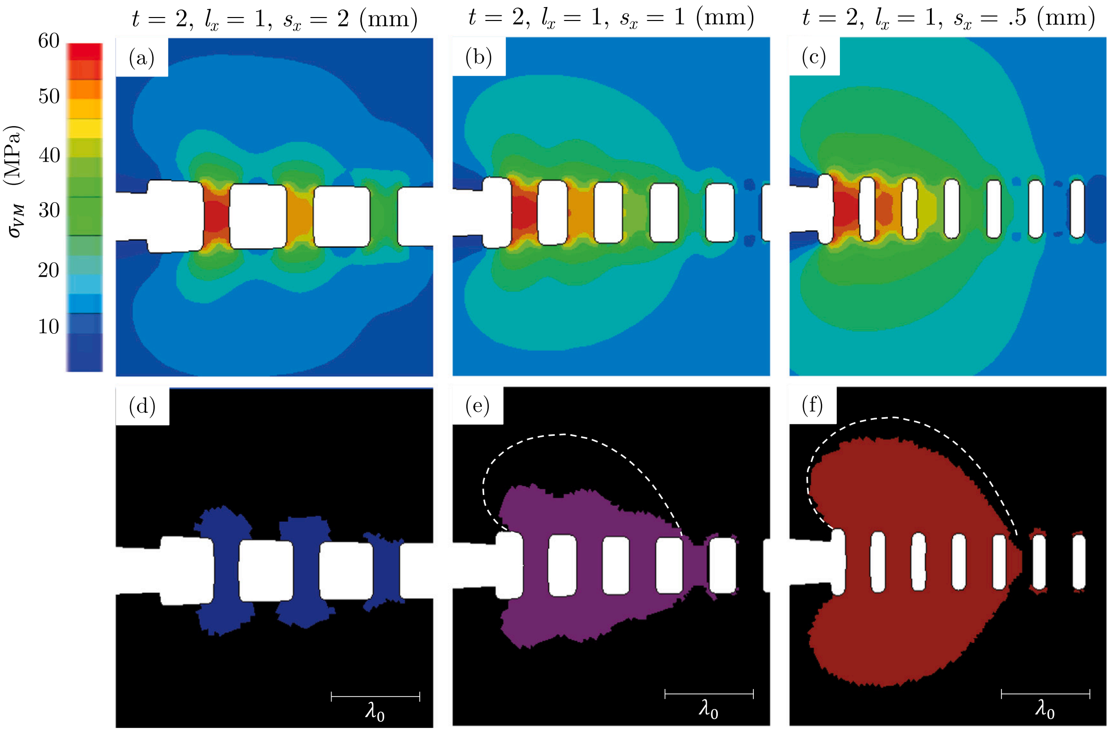

Fig. 4. Finite element simulations of three representative geometries, with pillar height $t = 2$ mm, pillar width $l_x = 1$ mm, and pillar spacings $s_x = 2$ (a & d), 1 (b & e), and 0.5 (c & f) mm. (a–c) show von Mises stresses in each geometry immediately before the first pillar fails. (d–f) show the regions of the specimens where the von Mises stress is greater than the yield strength (i.e., the plastic zone). Plastic zones are compared for the specimens immediately before failure of the first pillar and the length of the plastic zone extension for the homogeneous specimen, λ_0 is indicated. In (e & f), the plastic radii predicted from the perturbation model (Eq. (6)) are shown.

image of the simulation after the plastic zone and using the Abaqus graphical feature to highlight all elements that were plastically deformed. All plastic zones were taken immediately before specimen failure (i.e., when the plastic zones are fully formed). The images were then analyzed using the open-source image processing tool, ImageJ-v1.53, to calculate the areas of the plastic zones. It is clear that, as the pillar spacing decreases, the plastic regions above the pillars merge into a continuous domain, with a large amount of plasticity observed as the pillars get very close together. This follows the assumptions of the theoretical model. In Fig. 4(e&f), the predicted bulk plasticity using the perturbation model is shown. It is apparent that the perturbation model shows much better agreement for Fig. 5(f) than (e). This is expected as Fig. 5(e) corresponds to the maximum pillar spacing that generates a continuous bulk plastic zone and is the limiting case of the perturbation model. For Fig. 5(f), the perturbation model and FE result match much more closely. No prediction is shown for case Fig. 5(d) as it does not have a continuous plastic zone.

The toughness is predicted to scale with the volume of the plastic zone (Eqs. (4) & (5)). The toughness for each pillar geometry is given in Fig. 5(a) as a function each geometry's plastic zone volume. All values are normalized by their corresponding value in the homogeneous case, given in Table 1. A linear fit with fixed slope of 1 results in an estimation of the non-plastic contribution, $\delta_e = 0.26$, with a 95% confidence interval of $0.20-0.31$, and a good quality of fit ($R^2 = 0.98$). Note that the prediction and confidence interval for δ_e is much smaller than the magnitudes of most of the effective toughness measurements, as assumed in the model. It is apparent that the plastic zone volume is the dominant indicator of toughness for these systems, with the results from the entire parameter space of geometries all roughly collapsing together.

The effective toughness for each geometry as a function of the plastic zone extension, $N_p l_x$, normalized by that of a homogeneous specimen, λ_0, is given in Fig. 6(a). Specimens with isolated pillar plasticity are noted by open markers. As expected, these results approximately follow a linear relationship (see Eq. (5)). A linear fit with fixed slope of 1 has $R^2 = 0.97$. However, specimens with bulk plasticity (closed markers), do not follow this trend and scale nonlinearly, as expected. This results in significant increases in toughness, such that a >3.5× toughness enhancement is achieved, compared to the homogeneous specimen. The highest-performing geometries have arrays with small relative spacings and tall pillars. The maximum benefit possible will be much higher than the result achieved here if taller pillars with smaller relative spacings are considered. However, this work only considered array geometries with dimensions comparable to the plastic radius of the homogeneous specimen, for which our models are expected to hold. Furthermore, there will likely be practical limitations on the feasible dimensions of the pillar arrays for most materials, such as the minimum resolution of the fabrication method or that the intrinsic material strength may be lowered for small-scale features, which would limit the possible benefits. The exact limits, however, would be material-specific and are not considered here. The

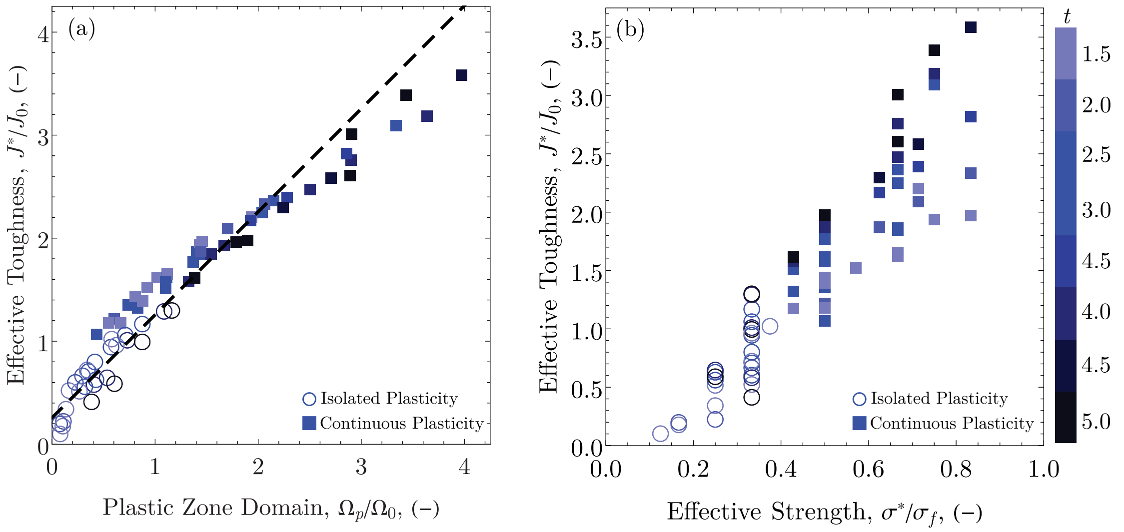

Fig. 5. (a) Effective toughness, J^*/J_0, as a function of plastic zone area, Ω_p, relative to a homogeneous specimen, Ω_0, with a linear fit following Eq. (4) included. (b) Effective toughness, J^*/J_0, as a function of effective strength σ^*/σ_f, which is equivalent to the pillar area fraction $f = l_x/(l_x + s_x)$. Open markers indicate geometries where isolated pillar plasticity is observed, and closed markers indicate unconfined plasticity.

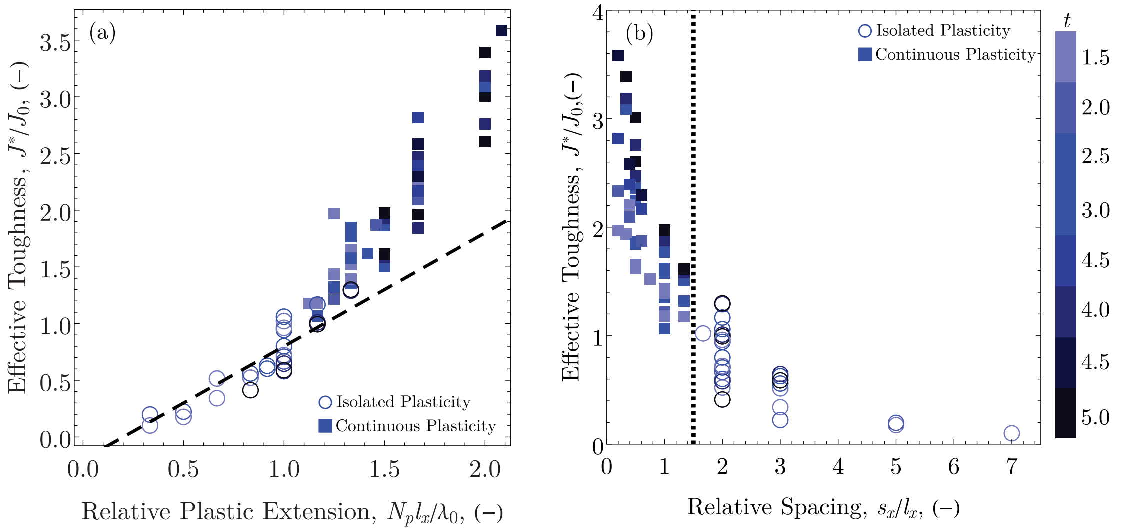

Fig. 6. (a) Effective toughness as a function of the relative plastic extension, $N_p l_x/\lambda_0$. Open markers indicate geometries where isolated pillar plasticity is observed, and closed markers indicate unconfined plasticity. A linear fit to the open markers is indicated, following Eq. (5). (b) Effective toughness vs. relative spacing of the pillars s_x/l_x. The dashed line indicates the transition point between the regimes is approximately at $s_x/l_x = 1.5$ (theoretical value is 1.2).

previous experimental work considering fracture of SLS PA 12 pillar arrays achieved a maximum increase in toughness of ∼2.25× relative to the homogeneous specimen.

The properties of the pillar array are considered relative to that of the solid material, and the enhancements in toughness are achieved by removing material. As noted in Eq. (22), this results in a reduction in strength. The effective tensile strength of all pillar arrays $\sigma^*/\sigma_f < 1$. However, there is no strict trade-off between strength and toughness in this system, unlike for homogeneous materials where any increase in strength or toughness usually results in a reduction in the other property. Fig. 5(b) shows the effective toughness versus the effective strength of the material, as predicted by Eq. (22). It is clear that toughness and strength are positively correlated in this system, with an increase in one value likely to result in an increase in the other. The two properties can also be tuned independently from one another. For a given strength, a range of toughness values can be achieved through choices in geometry. As noted in Fulco et al. (2022), one clear factor is pillar height, which can be changed independently from the strength of the system, but affects the toughness. Changes in pillar width and spacing will affect both properties, but the relationship is not uniform, as certain pillar widths and spacings will result in significant plasticity in the bulk, enhancing the toughness more.

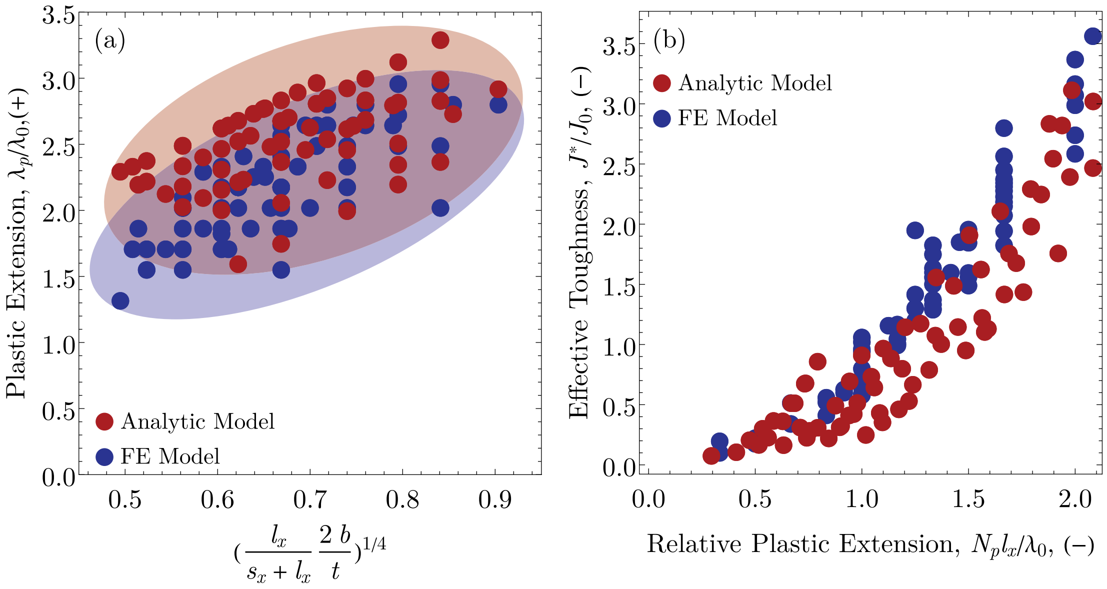

Fig. 7. (a) The plastic extension, normalized by that of a homogeneous specimen for both the analytical foundation model and the finite element simulations, versus a geometric parameter corresponding to the eigenvalue in Eq. (12). (b) Effective toughness, relative to a homogeneous specimen, versus the relative plastic extension for the finite element simulations and the model.

Fig. 6(b) shows the toughness for the relative spacing s_x/l_x. The results indicate if there was a continuous plastic zone (closed markers) like in Fig. 4(e,f), or isolated plasticity (open markers), like in Fig. 4(d). The geometry of the plastic zone for all simulations was identified from the image, as in Fig. 4. It is clear that there is a distinct transition between the two regimes around $s_x/l_x = 1.5$, as indicated by the dashed line in Fig. 6(b). This agrees reasonably with the prediction of the critical spacing value from the previous analysis ($s_c = 1.2l_x$). It is also apparent that the largest increases in toughness occur in the cases where significant plasticity in the bulk exists, as would be expected.

Since the predicted critical spacing value was found to be accurate and that the toughness followed closely to Eq. (4), the algorithm shown in Fig. 3 should be able to predict the toughness directly given the pillar geometry. Fig. 7(a) shows the plastic extension, normalized by that of a homogeneous specimen, predicted by the foundation model and the finite element analysis, as a function of the dimensionless eigenvalue of the foundation model, $\Lambda^{1/4} = (\frac{l_x}{s_x+l_x}\frac{2b}{t})^{1/4}$. It is clear that the two predictions are close, with the foundation model typically predicting slightly longer extensions, as expected. The predicted toughness results from the algorithm and Eq. (4) are shown in Fig. 7(b), where the effective toughness is shown as a function of the plastic extension. The finite element results and the results predicted by the algorithm are shown and match very closely. The algorithm provides no way of predicting δ_e, so this is taken as 0 since the effect is expected to be small (finite element results predict $\delta_e = 0.26$, as noted above). Overall, the model works very well to predict the toughness and suggests that the toughness for any pillar array could be accurately estimated.

While this work used a pillar array as a model system, the analytical model was essentially agnostic to the geometry and micromechanics of structure and depended only on the effective stiffness and strength of the structure. Investigation of other structures is outside of the scope of this work, but we suggest that the approach presented here, coupled with additional micromechanical analyses of other structures to determine the effective mechanical properties from geometry, could be used to predict the elastic–plastic fracture behavior of other structures.

This model does have some limitations, such as those previously noted (over-prediction of the plastic extension, no way to determine δ_e), but we also note that the perturbation analysis for predicting the bulk plastic area does not account for details of the process zone, such as the local affects near the pillar corners. The model also predicts an increased area of damage behind the crack tip ($\frac{\pi}{2} \leq \theta \leq \frac{3\pi}{2}$). While there will likely be some increase in plastic zone volume in this region due to the stress concentrations at the pillar corners, predicting the precise effect here is difficult and small errors may be accumulated in this region. These details contribute to the small discrepancies seen in the results compared to the finite element simulations.

5. Case study: Designing for non-similar crack growth

In the previous results, an assumption was made of a constant pillar geometry, which meant $\frac{d}{da}\left[\Omega_p\right] = 0$, which we referred to as self-similarity of the fracture process. While significant increases in toughness were achieved for repeating arrays, further opportunity exists in choosing a varying pillar geometry, where the derivative of the plastic integral is no longer constant, resulting in changing fracture properties as the crack propagates. As case studies, we present two geometries, one where pillar height increases from 2 mm

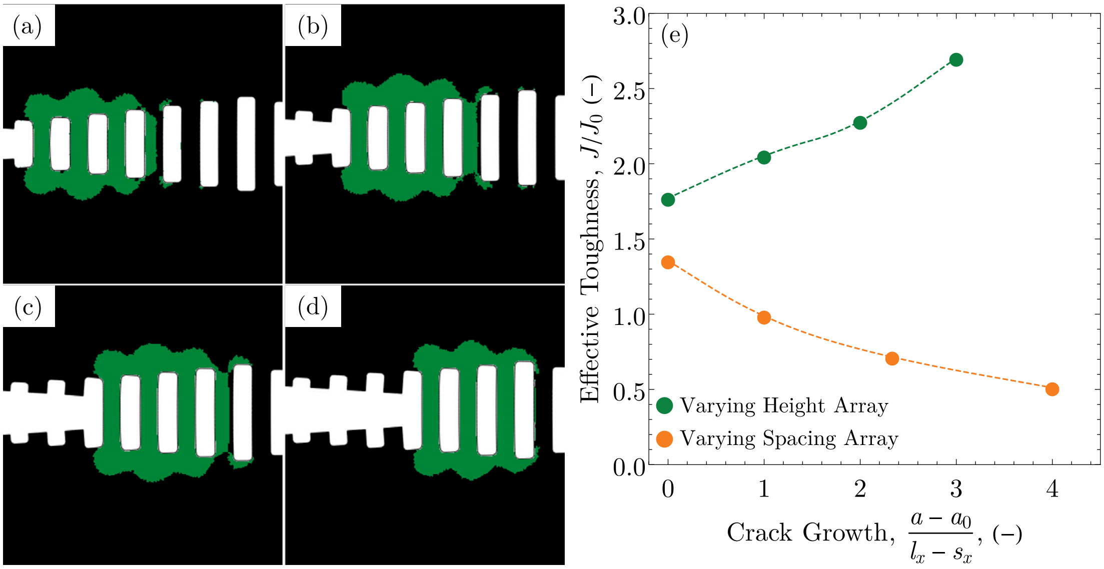

Fig. 8. (a–d) Plastic zones preceding failure of pillars 1–4, respectively, for the case of varying pillar height. Pillar height increases from 2 mm to 5 mm (in 0.5 mm increments). (e) Effective toughness, J, normalized by the experimental homogeneous value, J_0, as the crack propagates for the cases of increasing pillar height and increasing pillar spacing. Dashed lines are added as a visual aid for the reader.

to 5 mm in increments of 0.5 mm ($s_x = l_x = 1$ mm throughout) to increase the toughness as the crack propagates, and one where pillar spacing increases from 0.5 mm to 2.5 mm in increments of 0.5 mm ($t = 2$ mm, $l_x = 1$ mm throughout), to reduce toughness as the crack propagates. This, in effect, creates either an increasing or decreasing R-curve, which is driven through geometry, rather than material properties. Rising R-curves can be beneficial so that if a structure begins to fail through fracture under load control conditions, stable or delayed fracture may be achieved, rather than unstable failure. While many materials exhibit non-flat R-curves, here the process is driven purely through geometry, which leverages the architected plastic zone to tune the fracture behavior.

Fig. 8(a–d) show the growing plastic zone volume as the crack propagates for the first case of increasing pillar height. Up until the plastic zone passes the tallest pillar, the toughness should be strictly increasing as the crack grows. This case was simulated using the same CT model as in previous simulations. To simulate crack propagation, which was not considered in the previous results, a sequence of four simulations were run, where each subsequent simulation deleted the front-most pillar, as if that pillar had failed. This approach may introduce small errors as they do not consider the elastic unloading of the failed pillars, but we expect these effects to be small. Toughness results for the two case studies are given in Fig. 8(e), and show the effective toughness as a function of crack growth (a dashed line is indicated between points as a guide to the reader). It is clear that, for the case of increasing pillar height, toughness increases as the crack propagates due to an increasing plastic zone size, while for the case of increasing pillar spacing, the toughness decreases. This is an example of an architected material with engineered fracture resistance.

6. Conclusion

Architecture at the crack tip is shown to control and alter the plastic zone size and shape, and can be exploited to enhance the effective fracture toughness. Analytical mechanics models predict the size and shape of the plastic zone for a pillar array from the geometry and material properties, allowing for a prediction of the effective toughness. This is verified through a series of finite element simulations, which match well with the analytical predictions of plastic zone shape, size, and the resulting toughness. Toughness is enhanced by >3.5× through proper choices of geometry with only a modest reduction in strength. The model is further extended to the case of non-regular array geometries with pillars of varying spacing and height, demonstrating how architecture can be used to tailor fracture properties along the crack path.

These results demonstrate how elastic–plastic pillar failure and plastic zone shape is influenced by local geometry, and results in altered, and in some cases significantly enhanced, toughness. A pillar array was presented as a model system, but the mechanics models are agnostic to the micromechanics of the geometry and depend instead on homogenized properties like stiffness and failure strength. This work acts as a framework for analyzing plastically-failing architected materials and can be extended to other geometries, such as the non-regular pillar array considered as a case study in this work, and more complicated geometries. The results are primarily geometrically controlled, meaning that they can be transferred to other materials with little modification. Understanding and leveraging the role of plasticity in architected materials is shown to be highly valuable, as the designs considered here achieved significant increases in toughness, with minimal loss of strength, and demonstrated tunable fracture properties along the crack path, driven through geometry.

CRediT authorship contribution statement

Sage Fulco: Conceptualization, Methodology, Investigation, Formal analysis, Writing – original draft, Writing – review & editing. **Michal K. Budzik:** Conceptualization, Formal analysis, Writing – review & editing, Supervision. **Kevin T. Turner:** Conceptualization, Formal analysis, Writing – review & editing, Supervision.

Declaration of competing interest

The authors declare that they have no known competing financial interests or personal relationships that could have appeared to influence the work reported in this paper.

Data availability

Data will be made available on request.

Acknowledgments

This research was funded primarily by the National Science Foundation (NSF), United States MRSEC program [awards DMR-1720530 and DMR-2309043]. MKB acknowledges Aarhus University Research Foundation (AUFF), Denmark [grant number 28653] and the Velux Foundations for support under the Villum Experiment program [VIL50302], and SF acknowledges support from the US Department of Defense (DoD) through the National Defense Science & Engineering Graduate (NDSEG) Fellowship Program, United States.

Appendix. Numerical model validation

Fig. 9(a) shows a representative SLS PA 12 pillar specimen tested in Fulco et al. (2022). All numerical models in this work use the constitutive behavior derived from SLS PA 12 as detailed in Table 1, as well as the same CT geometry and overall dimensions. Fig. 9(b) shows the load–displacement curves for an experimental specimen tested in Fulco et al. (2022) and an FE model for a pillar array, both having dimensions $l_x = s_x = 1$ mm, and $t = 2$ mm. Data for the finite element model up to the peak load was derived from one simulation that followed the process described in Section 3. The final data point was derived from a second simulation where the front-most pillar was deleted, following the process described in Section 5. The small discrepancy in stiffness between the FE and experimental results for small displacements is due to the small bonded ligament ahead of the first pillar in the experimental specimen, which was not present in the FE model. When this ligament fails at ~900 N, the FE model and experimental specimens have identical geometries and the stiffness and peak load match closely. The second FE simulation also accurately captures the drop in critical load as the crack begins to propagate (i.e., as pillars fail), demonstrating the fidelity of the FE model to the experimental material.

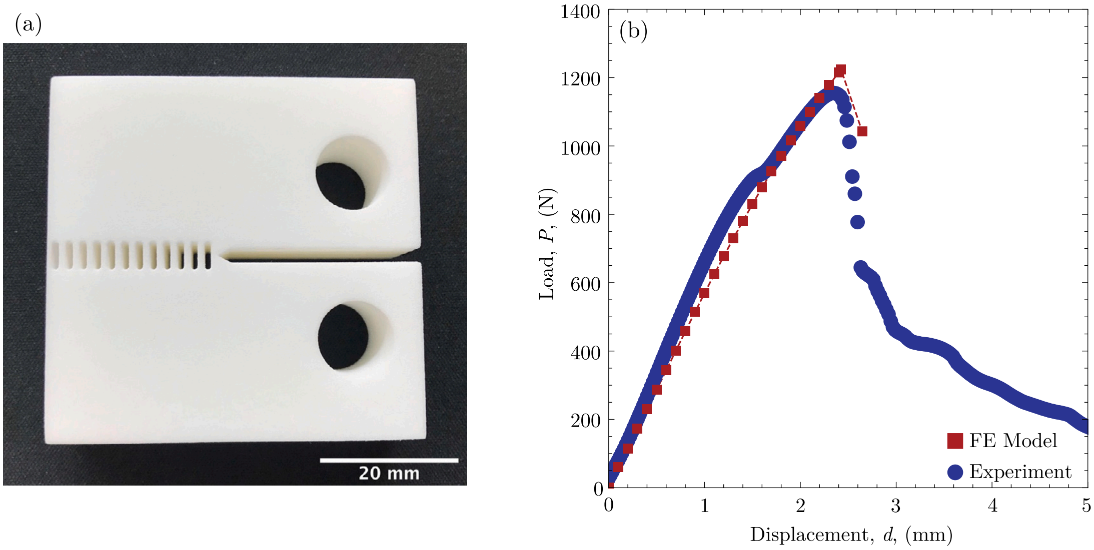

Fig. 9. (a) Representative experimental pillar CT specimen tested in Fulco et al. (2022). (b) Load–displacement data for an experimental specimen from Fulco et al. (2022) and an FE model from this work for CT specimens with a pillar array $l_x = s_x = 1$ mm and $t = 2$ mm. The final FE data point is derived from a second simulation where the front-most pillar is deleted. A dashed line is added to the FE data as a visual aid to the reader.

References

Abedi, M.M., Nedoushan, R.J., Yu, W., 2021. Enhanced compressive energy absoprtion properties of braided lattice and polyurethane foam hybrid composites. Int. J. Mech. Sci. 207, 1–16.

Ashby, M.F., 2005. The properties of foams and lattices. Philos. Trans. R. Soc. Lond. Ser. A Math. Phys. Eng. Sci. 364, 15–30.

ASTM, 2020. E399-20a: Standard Test Method for Linear-Elastic Plane Strain Fracture Toughness of Metallic Materials. ASTM.

ASTM International, 2007. ASTM D5045-99: Standard Test Methods for Plane-Strain Fracture Toughness and Strain Energy Release Rate of Plastic Materials. ASTM International, West Conshohocken, PA, USA.

Athanasiadis, A., Dias, M., Budzik, M., 2021. Can confined mechanical metamaterials replace adhesives? Extreme Mech. Lett. 48.

Bauer, J., Schroer, A., Schwaiger, R., Kraft, O., 2016. Approaching theoretical strength in glassy carbon nanolattices. Nature Mater. 15.

Bertoldi, K., Vitelli, V., Christensen, J., van Hecke, M., 2017. Flexible mechanical metamaterials. Nature Mater. 2.

Compton, B., Lewis, J., 2014. 3D-printing of lightweight cellular composites. Adv. Mater. 26.

Cui, Y., Gao, Y., Chew, H., 2020. Two-scale porosity effects on cohesive crack growth in a ductile media. Int. J. Solids Struct. 200–201.

Dillard, D.A., Mukherjee, B., Karnal, P., Batra, R.C., Frechette, J., 2018. A review of Winkler's foundation and its profound influence on adhesion and soft matter applications. Soft Matter 14, 3669–3683.

Fulco, S., Budzik, M.K., Bain, E.D., Turner, K.T., 2022. Decoupling toughness and strength through architected plasticity. Extreme Mech. Lett. 57.

Gao, Y., Bower, A., 2004. A simple technique for avoiding convergence problems in finite element simulations of crack nucleation and growth on cohesive interfaces. Modelling Simul. Mater. Sci. Eng. 12.

Griffith, A.A., 1921. VI. The phenomena of rupture and flow in solids. Philos. Trans. R. Soc. Lond. Ser. A Math. Phys. Eng. Sci. 221 (582–593), 163–198.

Gross, A., Bertoldi, K., 2019. Additive manufacturing of nanostructures that are delicate, complex, and smaller than ever. Small 15.

Heide-Jørgensen, S., Budzik, M., 2017. Crack growth along heterogeneous interface during the DCB experiment. Int. J. Solids Struct. 120.

Heide-Jorgensen, S., Budzik, M.K., Turner, K.T., 2020. Mechanics and fracture of structured pillar interfaces. J. Mech. Phys. Solids 137, 1–20.

Hossain, M., Hsueh, C.-J., Bourdin, B., Bhattacharya, K., 2014. Effective toughness of heterogeneous media. J. Mech. Phys. Solids 71.

Hsueh, C.-J., Avellar, L., Bourdin, B., Ravichandran, G., Bhattacharya, K., 2018. Stress fluctuation, crack renucleation and toughening in layered materials. J. Mech. Phys. Solids 120.

Irwin, G.R., 1957. Analysis of stresses and strains near the end of a crack transversing a plate. Trans. ASME Ser. E 24, 361–364.

Kanninen, M., 1973. An augmented double cantilever beam model for studying crack propagation and arrest. Int. J. Fract. 9 (1), 83–92.

Luan, S., Chen, E., Gaitanaros, S., 2022. Energy-based fracture mechanics of brittle lattice materials. J. Mech. Phys. Solids 169.

Lubliner, J., 1990. Plasticity Theory. Macmillan Publishing Co..

Mateos, A.J., Huang, W., Zhang, Y., Greer, J.R., 2019. Discrete-continuum duality of architected materials: Failure, flaws, and fracture. Adv. Funct. Mater. 29, 1–7.

Messner, M., 2016. Optimal lattice-structured materials. J. Mech. Phys. Solids 96.

Meza, L.R., Das, S., Greer, J.R., 2014. Strong, lightweight, and recoverable three-dimensional ceramic nanolattices. Science 345 (6202), 1322–1326.

Mohsenizadeh, M., Gasbarri, F., Munther, M., Beheshti, A., Davami, K., 2018. Additively-manufactured lightweight metamaterials for energy absorption. Mater. Des. 139.

Mueller, J., Raney, J., Shea, K., Lewis, J., 2018. Architected lattices with high stiffness and toughness via multicore–shell 3D printing. Adv. Mater. 30.

Muro-Barrios, R., Cui, Y., Lambros, J., Chew, H., 2022. Dual-scale porosity effects on crack growth in additvely manufactured metals: 3D ductile fracture models. J. Mech. Phys. Solids 159.

O'Masta, M., Dong, L., St-Pierre, L., Wadley, H., Deshpande, V., 2017. The fracture toughness of octet-truss lattices. J. Mech. Phys. Solids 98.

Ostoja-Starzweski, M., 2002. Lattice models in micromechanics. Appl. Mech. Rev. 55.

Park, S.J., Shin, J., Magagnosc, D., Kim, S., Cao, C., Turner, K., Purohit, P., Gianola, D., Hart, A.J., 2020. Strong, ultralight nanofoams with extreme recovery and dissipation by manipulation of internal adhesive contacts. ACS Nano 14.

Pham, M., Liu, C., Todd, I., Lertthanasarn, J., 2019. Damage-tolerant architected materials inspired by crystal microstructure. Nature 565, 305–313.

Ramachandramoorthy, R., Mieszala, M., Manzano, C.V., Maeder, X., Michler, J., Philippe, L., 2020. Dual-templated electrodeposition and characterization of regular metallic foam based microarchitectures. Appl. Mater. Today 20, 100667.

Ritchie, R.O., 2011. The conflicts between strength and toughness. Nature Mater. 10, 817–822.

Saccone, M., Gallivan, R., Narita, K., Yee, D., Greer, J., 2022. Additive manufacturing of micro-architected metals via hydrogel infusion. Nature 612.

Salem, N., Budzik, M., Jumel, J., Shanahan, M., 2013. Investigation of the crack front process zone in the double cantilever beam test with backface strain monitoring technique. Eng. Fract. Mech. 98.

Schaedler, T., Jacobsen, A.J., Torrents, A., Sorensenm, A.E., Lian, J., Greer, J., Valdevit, L., Carter, W., 2011. Ultralight metallic microlattices. Science 334 (6058), 962–965.

Shaikeea, A.J.D., Cui, H., O'Masta, M., Zheng, X.R., Deshpande, V.S., 2022. The toughness of mechanical metamaterials. Nature Mater. 21 (3), 297–304.

Timoshenko, S., Goodier, J., 1934. Theory of Elasticity, third ed. McGraw-Hill Book Company, Inc..

Vyatskikh, A., Delalande, S., Kudo, A., Zhang, X., Portela, C., Greer, J., 2018. Additive manufacturing of 3D nano-architected metals. Nature Commun. 9.

Walia, S., Shah, C., Gutruf, P., Nili, H., Chowdhury, D., Withayachumnankul, W., Bhaskaran, M., Sriram, S., 2015. Flexible metasurfaces and metamaterials: a review of materials and fabrication processes at micro- and nano-scales. Appl. Phys. Rev. 2.

Wegst, U., Bai, H., Saiz, E., Tomsia, A., Ritchie, R., 2014. Bioinspired structural materials. Nature Mater. 14.

Yang, Y., Dias, M., Holmes, D., 2018. Multistable kirigami for tunable architected materials. Phys. Rev. Mater. 2.

Zhang, L., Mao, X., 2018. Fracturing of topological maxwell lattices. New J. Phys. 20, 1–11.

Zheng, X., Lee, H., Weisgraber, T.W., Shusteff, M., Dotte, J., Duoss, E., Kuntz, J.D., Biener, M., Ge, Q., Jackson, J., Kucheyev, S., Fang, N., Spadaccini, C.M., 2014. Ultralight, ultrastiff mechanical metamaterials. Science 344 (6190), 1373–1377.